Realizing topological edge states in graphenelike elastic metamaterials

Zhen Huang,[1,2,§] Penglin Gao,[3,§] Federico N. Ramírez,[4] Jorge García-Tíscar,[4] Alberto Broatch,[4] Jiu Hui Wu,[2,*] Fuyin Ma,[2,†] and José Sánchez-Dehesa[1,‡]

[1] *Wave Phenomena Group, Department of Electronic Engineering, Universitat Politècnica de València, Camino de vera s.n. (Building 7F), ES-46022 Valencia, Spain*

[2] *School of Mechanical Engineering, Xi'an Jiaotong University, Xi'an 710049, China*

[3] *School of Mechanical Engineering and State Key Laboratory of Mechanical System and Vibration, Shanghai Jiao Tong University, Shanghai 200240, China*

[4] *CMT − Clean Mobility & Thermofluids, Universitat Politècnica de València, Camino de vera s.n. (Building 6D), ES-46022 Valencia, Spain*

The study of topological states, which allow transport properties that are robust against impurities and defects in electronic structures, has been recently extended to the realm of elasticity. This work shows that nontrivial topological flexural edge states located on the free boundary of the elastic graphenelike metamaterial can be realized without breaking the time-reversal, mirror, or inversion symmetry of the system. Numerical calculations and experimental studies demonstrate the robust transport of flexural waves along the boundaries of the designed structure. The topological edge states on the free boundary are not limited by the size of the finite structure, which can reduce the scale of the topological state system. In addition, unlike the edge states localized on the free boundary in graphene where the group velocity is zero, the edge states on the elastic metamaterial plate have propagation states with nonzero group velocity. We have introduced the concept of Shannon entropy for elastic waves to assess the frequency range of the edge states in graphenelike elastic metamaterials. This work represents a relevant advance in the study of elastic wave topological states, providing a theoretical basis for engineering applications such as vibration reduction and vibration isolation for mechanical structures.

I. INTRODUCTION

Mechanical vibrations are ubiquitous in many circumstances related to our daily lives, such as high-speed trains, airplanes, subways, and other means of transportation. At low frequencies, the excited elastic waves usually produce non-negligible damage to the embedded mechanical devices. Therefore, the design of novel structures to control elastic wave propagation acquires paramount relevance. In this regard, elastic metamaterials are new artificial structures that show exciting properties, including wave transformation [1–3], negative refraction [4,5], focusing, and elastic cloaking [6,7]. As a consequence, the research on elastic metamaterials has been rapidly developed in the last few years.

Topological states were initially studied in condensed matter physics, since they exhibit novel properties, such as topologically protected one-way energy propagation without loss and backscattering [8–15]. This property, combined with the specific features of elastic metamaterials, aroused the interest of researchers for extending topological states to the realm of elasticity. Thus, the study of topological materials for elastic waves has emerged as a novel research topic in elasticity.

In the field of electronic structures, research on topological states mainly focuses on the quantum Hall effect (QHE) [8,14], the quantum spin Hall effect [10,15–18], and the quantum valley Hall effect (QVHE) [11,12]. Among them, the key to observing the QHE is the breaking of the time-reversal symmetry [8,14]. In the field of elastic structures, in order to break the time-reversal symmetry, the elastic analogue of the QHE employs moving elements added to the system, such as a rotating gyroscope introduced at each site of the lattice [19,20]. However, the effects brought about by active control systems, such as instabilities and noise, are unavoidable and hinder potential engineering applications. As a result, passive metamaterials are gradually being introduced into the study of topological states [21]. For example, both topological insulators with pseudospin-orbit coupling and valley topological insulators with pseudospin states rely on the passive

---

*Corresponding author: ejhwu@xjtu.edu.cn

†Corresponding author: xjmafuyin@xjtu.edu.cn

‡Corresponding author: jsdehesa@upv.es

§These authors contributed equally to this work

properties of metamaterials without breaking the time-reversal symmetry. For the former, spin-orbit coupling is the key ingredient to generating a pair of conjugated topological edge states with opposite spins and protected by time-reversal symmetry [22–29]. As for the QVHE, which was derived from single-valley physics in the realm of elastic waves [26], an effective strategy to open a topologically nontrivial band gap is using point group symmetry conditions [27–33]. It should be noted that the realization of topological states in metamaterials commonly relies on domain walls, which serve as the essential framework for the existence of topological states [34].

In short, the realization of topological states in elastic wave systems requires active or passive methods to change the time-reversal symmetry or the lattice symmetry of crystals to obtain the nontrivial topological phases, which can be quantified by topological invariants such as Chern numbers or (valley) spin Chern numbers. Topological edge states typically emerge within the topological band gap and are often localized at the interface between two distinct topological phases [26,31,35]. Therefore, achieving topological states at the free boundaries of a system is generally challenging. To address this challenge, Wu *et al.* [27] reported a three-dimensionally metal-printed bilayer metamaterial utilizing chiral interlayer coupling to open a topologically nontrivial band gap, realizing topological states localized at the free boundary of a single topological phase. In addition, previous research on topological states of elastic waves focused on realizing topological band gaps, such as by reducing the symmetry of the system, changing the distribution of the eigenmode field of the system, or producing an effective synthetic gauge flux in the structure. In fact, topological phase transitions can also be generated with the band gap closed, such as with the graphene structure in an electronic system; a semi-infinite and a gapless graphene sheet with a zigzag edge has a band of zero-energy states localized at the edge [36–38]. The elastic analogue was theoretically proposed in 2013 using a simple model consisting of a honeycomb distribution of mass-spring resonators on top of a thin plate [37]. Its realization in an actual elastic plate would be of great interest to prove the transmission through edge states in a gapless structure.

Here, we demonstrate the feasibility of topologically protected edge states in a graphenelike elastic metamaterial, without breaking the time-reversal, mirror, or inversion symmetry of the system. Edge states appear at the free borders of the system rather than on domain walls formed by metamaterials with different topological phases, producing a significant reduction in the system size and holding great potential for device application. At the frequency of the Dirac point in structures formed by zigzag boundaries, we find frequency bands composed of edge states. Then, by analogy with the electronic propagation in graphene, we confirm that the edge states on the

bands have nontrivial topological phases by mapping them to a one-dimensional (1D) lattice with chiral symmetry. Numerical calculations and experimental data show that there is a range of frequencies where edge states can be excited in the graphenelike elastic metamaterial ribbon. In addition, to measure the frequency range where edge states occur in the graphenelike elastic plate, we introduce the concept of elastic Shannon entropy. To the best of our knowledge, the phenomenon of topologically protected flexural wave transport in graphenelike elastic plates has not yet been seen.

II. TOPOLOGICAL STATES IN THE GRAPHENELIKE METAMATERIAL PLATE

A. Topological states on the boundary

To construct acoustic or elastic topological states in phononic crystals, it is generally necessary to first realize different topological phase systems through band inversion, and then select two phononic crystals with overlapping bulk band gaps before and after the band inversion, and the topological states are then localized on the interface (domain wall) composed of the two phononic crystals with distinct topological phases [34,39,40], as shown in Fig. 1(a). Therefore, the realization of the topological states at the free boundary of the nondomain wall system is helpful to reduce the size of the topological material and improve the utilization ratio of the material. Under the condition that the system time-inversion symmetry is intact while the space-inversion symmetry is broken, there are two main schemes to realize topological states at the free boundary of the elastic system. One is to fold the system containing the domain wall along the interface so that the topological states appear at the free boundary, as shown in Fig. 1(b); the other is to use interlayer coupling to realize topological states at the free boundary of the single-phase system [27]. Among the two methods, the former is a complex system containing a domain wall, while the latter is implemented in a single-phase system that breaks space-inversion symmetry. Therefore, further research should be performed with new proposals allowing topologically protected edge states on the free boundaries of simple elastic systems without breaking the time- or space-inversion symmetry of the nondomain wall system, as shown in the lower panel of Fig. 1(b), to simultaneously reduce the size of the structure for miniaturization purposes and improve its integration.

B. Elastic analogue of graphene

The electronic properties of graphene, such as the integer QHE and the lossless supercurrent, have been attracting intense interest. These effects are a consequence of the electronic band structure of graphene, which consists of two Dirac cones at the K and K' points in the k space,
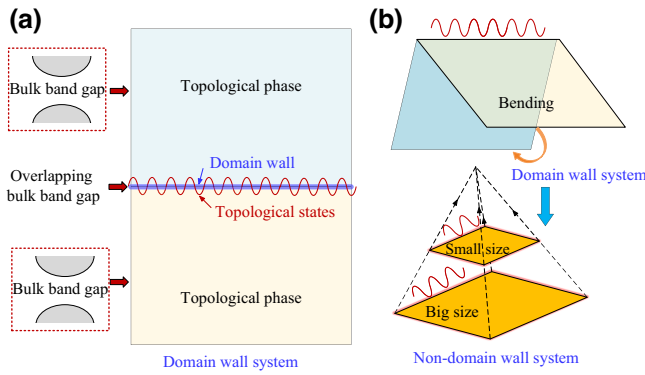
FIG. 1. (a) Schematic pictures representing a topological nontrivial system with domain walls. The phononic crystals on both sides of the domain wall contain a bulk band gap with the same or similar frequency range but different topological phases. This band gap supports topological edge states localized on the domain wall. (b) Sketches illustrating the topological state propagation in a folded system of elastic crystals along the domain wall and the case on the free boundary of a simple system. The upper panel represents the folded system, while the lower panel represents the simple nondomain wall system, where the dashed arrows indicate the direction in which the big simple system can be reduced to a small one.

as shown in Fig. 2. A graphite sheet behaves like a gapless semiconductor due to the electronic modes, which are called edge states, localized near the zigzag edge of graphene [38,41]. These localized electronic states correspond to nonbonding molecular orbitals [42]. The edge states could also exist near the zigzag end of a single-wall carbon nanotube since a carbon nanotube can be considered a graphene sheet wrapped into a cylinder [41]. Researchers have explored the zero modes of the graphene tube and found that two perfect midgap edge states exist, in which the particle is completely located at the boundary, even for a tube with finite length [43,44].

The edge states in the graphene model are caused by the chiral symmetry of the Hamiltonian and are related to the Dirac cone [45,46]. Therefore, we can extend the graphene edge states in electrons to elastic waves in solids with a honeycomb lattice, based on the Dirac cones at high-symmetry points K and K' in the Brillouin zone (BZ). Dirac cones are characterized by two principal features: the double degeneracy and linear dispersion near the degenerate point, which both depend on the symmetry of the crystal lattice [47,48]. However, because of the full-vector feature and the complicated couplings between the longitudinal and transverse components of elastic waves, manipulating elastic waves in solids, such as rapidly decaying wave amplitude from a solid boundary to the interior, is generally challenging [27]. Our work mainly considers the edge states of flexural waves in thin plates with a triangular lattice with symmetry operations of the C_{3v}

group, as shown in Fig. 2. In this case, we can concentrate the vibration of the elastic plate on the edge, and the vibrational energy is rapidly attenuated with the distance to the edge, as depicted schematically by the blue curve in Fig. 2.

C. Band structure of the unit cell

Let us consider an elastic plate patterned with a periodic array of hexagonal holes containing three one-beam resonators equally distributed inside the hexagonal cavity, as shown in Fig. 3(a). We select this unit cell since their parameters can be adjusted to obtain specific properties of the flexural band structure [27]. The upper and lower panels show top and cross-sectional views of the unit cell, respectively. The lattice constant of the cell is a. Other geometric parameters include the plate thickness h, radius R of the inscribed circle in the hexagonal hole, diameter d of the cylindrical pillar, cylinder height t outside the plate, width w_b of the beam, and the center moment ℓ of the beam.

In order to study the effects of the one-beam resonators on the band structure, we first analyze the dispersion relation of the unit cell without resonators, which is shown in Fig. 3(b). The hexagon in Fig. 3(b) represents the first BZ, whereas the orange region M-K-Γ-M represents the irreducible BZ. The bottom inset depicts a scheme of the unit cell. This work mainly analyzes the propagation behavior of the flexural wave in the elastic plate. The governing equation for the displacement of the triangular lattice plate is [27] $(\lambda + \mu)\nabla(\nabla \cdot \mathbf{U}) + \mu\nabla^2\mathbf{U} = \rho\ddot{\mathbf{U}}$, where λ and μ are Lamé constants, $\mathbf{U}(x,y,z) = u\mathbf{i} + v\mathbf{j} + w\mathbf{k}$ denotes the displacement vector, and ρ is the material density. Therefore, we define the out-of-plane polarization ratio D_Z to distinguish the flexural modes, which can be calculated as
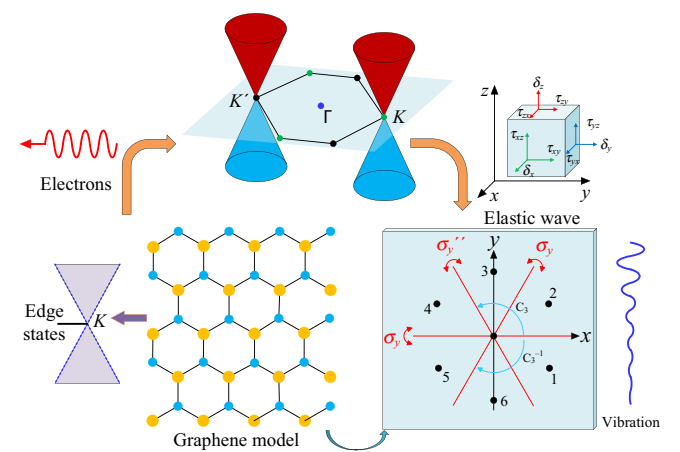

FIG. 2. Schematic diagram showing the analogy between graphene edge states and elastic systems.
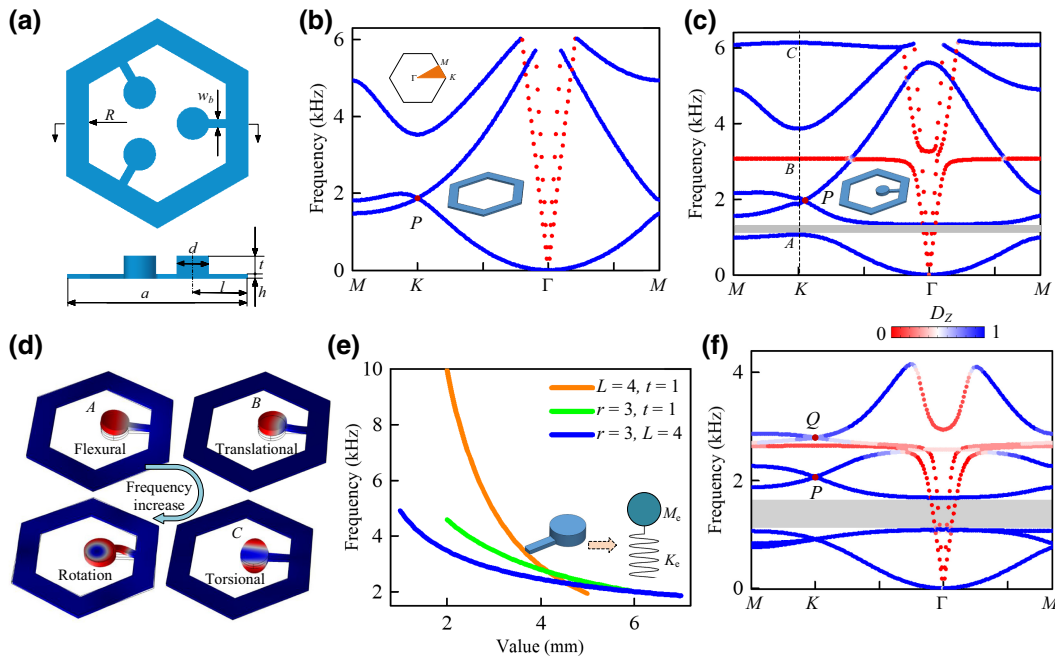
FIG. 3.   (a) Schematic diagram of the unit cell with the definition of its geometrical parameters. The upper figure shows a top view, and the lower figure is a cross-sectional view. (b) Band structure of a unit cell without the three-beam resonators. The upper inset depicts the first Brillouin zone, and the lower represents the cell. The blue and red dotted lines indicate the out-of-plane and the in-plane modes, respectively. (c) Band structure of a hexagonal lattice where the unit cell contains a one-beam resonator as described in the inset. (d) Displacement field distributions for the eigenmodes of local resonances *A*, *B*, and *C* in (c). The blue arrow indicates the modes with increasing frequency. (e) The behavior of the midfrequency resonant band gap produced by the one-beam resonator embedded in the unit cell. The inset represents the one-beam resonator, which is made equivalent to a spring-mass system. (f) Band structure corresponding to the unit cell shown in (a).

follows [49]:

$$D_Z = \frac{\int_V z^2 dV}{\int_V (x^2 + y^2 + z^2) dV},$$

where x, y, and z are the components of displacement along the x, y, and z directions, respectively. The symbol V represents the volume of the unit cell. The parameter D_Z takes values from 0 to 1. When the value D_Z is close to 1, it means that the vibration of the elastic plate is a pure flexural wave. However, when D_Z is close to 0, it means that the vibrations are in the plane. See Appendix A for further details of the numerical simulation and the convergence of the calculated frequencies. Blue and red dotted lines represent the out-of-plane and in-plane modes, respectively, in the band structures shown in Fig. 3. Figure 3(b) shows that a deterministic Dirac cone arises at the corner K in the BZ because of the C_{3v} symmetry of the unit cell, and there is another Dirac point at K' derived directly from time-reversal symmetry [39]. However, the Dirac point P is not at the valley of the two related bands, so an additional structure should be proposed to accomplish such a condition.

To adjust the band structure, we use the known properties of local resonance excited by a lattice of

one-beam resonators [50]. Figure 3(c) represents the band structure calculated with the unit cell shown in the inset. It is observed that the Dirac point P at the band valley still exists, but it deviates from the corner of the BZ because of the reduced lattice symmetry. It is worth noting that compared with Fig. 3(b), the band structure in Fig. 3(c) shows three additional bands caused by the lattice of one-beam resonators, and all of them contain frequencies where the dispersion relations are flat due to the lattice of local resonances (see Appendix B). To study the characteristics of these three extra bands, we study the band eigenmodes at the positions named *A*, *B*, and *C* in Fig. 3(c), which are all located at the corner K of the BZ. Figure 3(d) plots the eigenmodes, showing that they correspond to fundamental modes of the one-beam resonators, i.e., flexural mode (*A*), translational mode (*B*), and torsional mode (*C*). In addition, Fig. 3(d) also depicts the spin mode *D*, which is located at a much higher frequency (not shown in the band structure). To decrease the frequency position of the Dirac point, we realize that the flexural band structure can be adjusted by just tuning the parameters defining the one-beam resonators. For example, for the band gap (gray area) in Fig. 3(c), a simple mass-spring-pendulum model can be used to explain its formation mechanism, i.e., due to the introduction of the pendulum, the resulting band structure

of the 1D system formed by the combination of mass and spring has two branches. Therefore, a gap appears between the maximum frequency of the first branch at the zone boundary and the lowest frequency of the second branch at the Γ point [51]. Furthermore, the central frequency of the resonance band gap can be obtained by modeling the one-beam resonator as a simple spring-mass structure [as shown in the inset in Fig. 3(e)], and the expression is

$$f_M = \frac{1}{2\pi}\sqrt{\frac{K_e}{M_e}},$$

where M_e and K_e represent the equivalent mass of the spring-mass oscillator and the equivalent stiffness of the spring, respectively. Since the beam is modeled as a spring, the equivalent mass is the mass of the cylinder at the end of the beam $M_e = \pi r^2(t+h)\rho$, where the radius of the pillar $r = d/2$. The stiffness of the equivalent spring is

$$K_e = EI\left(\frac{1}{2}L_0 L^2 - \frac{1}{6}L^3 + (L_0 - L)\left(L_0 L - \frac{1}{2}L^2\right)\right)^{-1},$$

where E is the Young's modulus, I represents the moment of inertia of the rectangular cross section beam $I = w_b h^3/12$, L is the effective length of the beam $L = l - r$, and L_0 represents the equivalent moment of the concentrated force action point $L_0 \in (l, l+r)$. Thus, the central frequency f_M of the band gap associated with one-beam local resonance can be approximated by the simple model.

To guarantee the robustness of the structure to be manufactured, we fix the width of the beam to the value $w_b = 2$ mm. Therefore, we study the dependence of f_M on the length L of the beam, the radius r of the disk, and the height t of the cylinder added on top of the disk. The orange curve in Fig. 3(e) indicates the dependence on the cylinder radius when $L = 4$ mm and $t = 1$ mm. The green curve depicts the dependence on L when $r = 3$ mm and $t = 1$ mm, and the blue curve represents the relationship between the extra height t of the cylinder and the intermediate frequency of the band gap when $r = 3$ mm and $L = 4$ mm. It is observed that f_M decreases with increasing L, r, and t. From the slopes of the three curves, the radius of the disk has the greatest influence on f_M, followed by the length of the beam, and finally, the height of the cylinder added to the disk.

To ensure that a deterministic Dirac point appears at point K, we employ the unit cell shown in Fig. 3(a), where three one-beam resonators are symmetrically distributed in the unit cell, so that the lattice and the high-symmetry point K have C_{3v} symmetry at the same time [47]. In this case, where three one-beam resonators are considered, the number of resonant modes is triple in comparison with the case of lattices with only a single one-beam resonator. To have the central frequency of the band gap f_M smaller than the

frequency of the Dirac point P in Fig. 3(b), we choose a set of parameters extracted from Fig. 3(e) (see Methods). Figure 3(f) shows the calculated band structure, where the Dirac point P, with frequency 2068.7 Hz, occurs at the high-symmetry point K. The local modes introduced by the three one-beam resonators produce three flexural flat bands at low frequencies. A band gap occurs between the lower two flat bands that are degenerated at the Γ point and the third one. The low-frequency band gap caused by local resonance can achieve the goal of low-frequency vibration reduction, so the thin plate considered here can be called an elastic metamaterial [6]. It is worth noting that there is another Dirac point Q at corner K. In comparison with the band structure associated with the single one-beam resonator case [see Fig. 3(c)], the additional Dirac point Q is caused by the in-plane (translational) resonant mode arising from the three one-beam resonators. The underlying physics involves the interaction of the in-plane mode and the flexural waves propagating in the plate, which produces a fully out-of-plane mode, defining a Dirac cone under the protection of structural symmetry.

D. Dispersion relation of ribbons

To analyze the edge states induced by Dirac cones, we realize that there are two types of interfaces in an infinite elastic metamaterial slab. Figure 4(a) shows a scheme of the sample containing the two kinds of interfaces: the armchair (AM) interface and the zigzag (ZZ) interface. First, let us study finite "ribbons" formed by the AM interfaces as shown in the supercell depicted in Fig. 4(b). The ribbon is considered periodic along the y axis, with lattice constant $s = \sqrt{3}a$. Figure 4(c) shows the calculated dispersion relation of the flexural modes (blue dotted lines) where an omnidirectional band gap of out-of-plane modes (gray stripe) appears around the frequency of the Dirac point. Since flexural waves with frequencies in the band gap cannot propagate in the ribbon, the calculated flexural modes correspond to states propagating in the bulk of the ribbon, and no edge states appear in this ribbon. Let us point out that in-plane modes (red dotted lines) can also propagate in the ribbon but they are of no interest to this work.

Next, we analyze ribbons with ZZ edges, which are obtained with the supercell shown in Fig. 4(d). The supercell is periodic along the x axis, with lattice period a. Figure 4(e) shows the corresponding dispersion relation for the flexural modes (blue dotted lines). It is observed that, in addition to the bulk modes, there is a pair of bands (DB1 and DB2) extending near the Dirac point, and near $k_x = 1$ the eigenmodes are localized on the free boundary, which are similar to the zero-energy modes in the graphene energy band structure [36,38,52]. We select two eigenmodes at $k_x = 0.94$ near the frequency of the Dirac point; as shown in Fig. 4(f), the out-of-plane displacements field
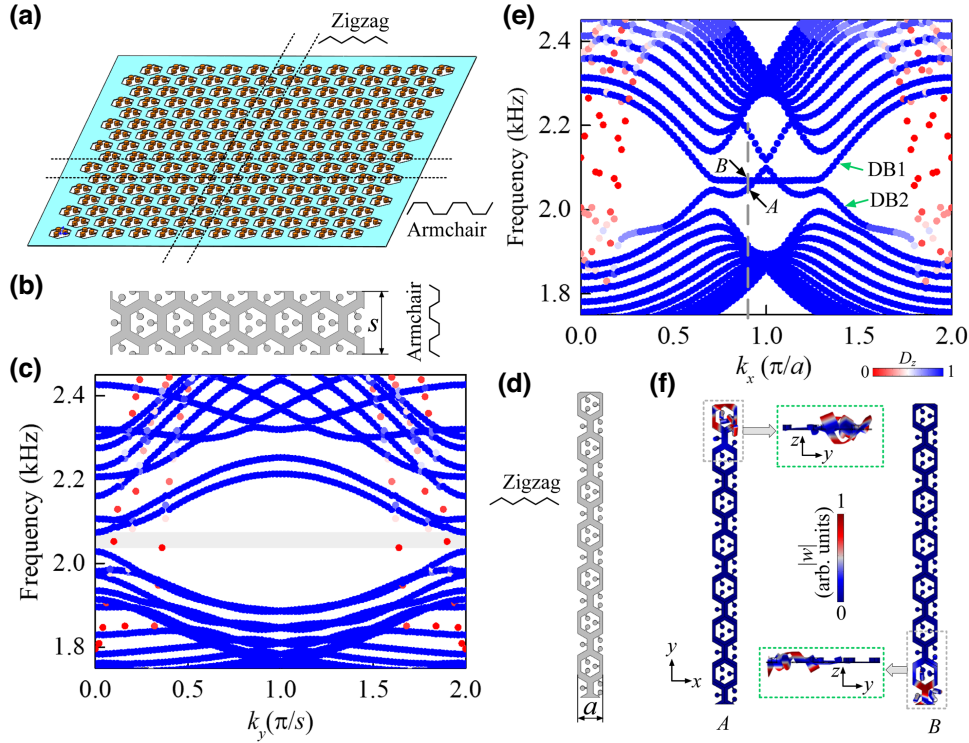
FIG. 4. (a) Plot of the designed metamaterial plate employed to study flexural edge states. (b) Ribbon containing armchair boundaries. (c) Dispersion relation of the projected bands corresponding to the ribbon described in (b). Blue dots in the band structure indicates out-of-plane modes, while red indicates in-plane modes. (d) Ribbon containing zigzag boundaries. (e) The dispersion relation for the ribbon (d). (f) Distribution of displacement field for the eigenmodes A and B at $k_x = 0.94$ in (e). Color represents the out-of-plane displacements field strengths $|w|$.

strengths $|w|$ of the two modes A and B exhibit a strong localization at the top and bottom end of the ribbon, respectively, decaying rapidly into the bulk of the ribbon. These localized modes have the features of a flexural wave [53], as shown in the green dashed box in Fig. 4(f). In addition, the characteristic of mode B on DB1 is that it is localized at the bottom end of the ribbon, while mode A on DB2 is localized at the top end of the ribbon. The emergence of edge states is related to the chiral symmetry of the Hamiltonian, and the choice of boundaries affects the chiral symmetry, thereby causing changes in the frequency band of the edge states. When there is strict chiral symmetry, there are two degenerate flat bands near $k_x = 1$, such as in graphene sheets [38]; while when the chiral symmetry is broken, the frequency band of the edge states disappears, such as in elastic granular graphene structures [54]. The choice of the boundary of the supercell affects the chiral symmetry of the Hamiltonian, reducing the strict chiral symmetry to the approximate chiral symmetry. As a result, in addition to the flat band in the frequency band of the edge states near $k_x = 1$, nonflat bands can also be observed. This indicates that the edge states still exist under the protection of the approximate chiral symmetry. Next, we study the topological properties of the edge states near the Dirac point frequency.

E. One-dimensional model and topological phase

To check that edge states have topological protection, the assessment method consists of calculating the topological phase in the corresponding frequency band. Typically, nontrivial topological phases of two-dimensional (2D) periodic structures are embodied in the band gap, and topologically protected states appear at the interface formed by phononic crystals of different topological phases [26]. Therefore, it is challenging to calculate the topological phases of gapless structures, due to the band degeneracy (Dirac cone) as in the case studied here. We adopt the winding number [44], which is an integer representing the total number of times that a closed curve travels counterclockwise around a given point so that the wave function remains unaltered, to discuss the topological arguments [53]. The left panel of Fig. 5(a) demonstrates a 2D infinite metamaterial plate. By equating the nonequivalent center points of the triangular lattice into lattice points [indicated by blue and yellow circles, respectively, in the middle panel of Fig. 5(a)], the triangular lattice can be converted into a honeycomb lattice [46]. The corresponding lattice vectors are $\mathbf{b}_1 = \left(1/2, \sqrt{3}/2\right) a$ and $\mathbf{b}_2 = \left(1/2, -\sqrt{3}/2\right) a$, and an elastic metamaterial

plate of the graphenelike model is obtained, which is called an elastic graphenelike sheet, as shown in the middle panel of Fig. 5(a). We cut a finite rectangular area with the boundary vectors $\mathbf{R}_{t1}$ and $\mathbf{R}_{t2}$ in the equivalent elastic graphene plate. The primitive vectors of the unit cells of the rectangular area are $\mathbf{R}_1 = n\mathbf{b}_1 + m\mathbf{b}_2$ and $\mathbf{R}_2 = p\mathbf{b}_1 + q\mathbf{b}_2$, respectively. By arranging the unit cells with base vectors $\mathbf{R}_1$ and $\mathbf{R}_2$ along the direction of the base vectors, a rectangular area can be obtained. In addition, in the honeycomb lattice, the basis vector of the primitive cell satisfies $|\mathbf{b}_1 \times \mathbf{b}_2| = |\mathbf{R}_1 \times \mathbf{R}_2|$, from which we can obtain the coefficient relationship $mp - nq = 1$. When the boundary vector $\mathbf{R}_{t1}$ of the rectangular area is parallel to the x-coordinate axis, we obtain $\mathbf{R}_1 = \mathbf{a}_1$, $\mathbf{R}_2 = \mathbf{a}_2$, where $\mathbf{a}_1$ and $\mathbf{a}_2$ are the two basis vectors of the honeycomb lattice unit cell, which is the same as the unit cell composed of $\mathbf{b}_1$ and $\mathbf{b}_2$. Then we can get $\mathbf{R}_1 = \mathbf{b}_2$, $\mathbf{R}_2 = \mathbf{b}_1$, and $m = p = 1$, $q = n = 0$, satisfying the coefficient relationship between unit cell basis vectors [46]. Therefore, the basis vectors of the rectangular area in the reciprocal space are $\mathbf{d}_1 = 2\pi/a \left(1, -1/\sqrt{3}\right)$ and $\mathbf{d}_2 = 2\pi/a \left(1, 1/\sqrt{3}\right)$, as shown in Fig. 5(b). In the finite rectangular area, to avoid the existence of a single-beam oscillator at the boundary and affecting the processing accuracy of the sample, we move the rectangular area a certain distance along the y axis. This movement will affect the chiral symmetry of the Hamiltonian; however, the edge states still exist under the protection of the approximate chiral symmetry [46].

For the honeycomb lattice, the Hamiltonian can be calculated based on the tight-binding model [45,52], which is $H(\mathbf{k}) = [0, g(\mathbf{k}); g^*(\mathbf{k}), 0]$. By considering only the relative phase to adjoining sites, the off-diagonal term of the Hamiltonian can be expressed as $g(\mathbf{k}) = 1 + e^{i\mathbf{k}\cdot(\boldsymbol{\delta}_3 - \boldsymbol{\delta}_2)} + e^{i\mathbf{k}\cdot(\boldsymbol{\delta}_3 - \boldsymbol{\delta}_1)}$, in which $\boldsymbol{\delta}_i$, $i = 1, 2, 3$ are the nearest-neighbor vectors [46]. The Bloch wave vector $\mathbf{k}$ should be expressed in accordance to the honeycomb lattice $\mathbf{k} = k_{\mathrm{h}}\mathbf{d}_1 + k_{\mathrm{v}}\mathbf{d}_2$, $k_{1,2} \in [0, 1)$. Substituting the expression for $\mathbf{k}$ into $g(\mathbf{k})$ finally gives rise to $g(k_{\mathrm{h}}, k_{\mathrm{v}})$. The two-by-two effective Hamiltonian $H(\mathbf{k})$ can be used to describe a 1D lattice model when k_{v} runs through the 1D BZ for each k_{h}. Thus, the winding number can be characterized by

$$v(k_{\mathrm{h}}) = \frac{1}{2\pi i} \int_0^0 \frac{\partial \ln[g(k_{\mathrm{h}}, k_{\mathrm{v}})]}{\partial k_{\mathrm{v}}} dk_{\mathrm{v}},$$

where $g(k_{\mathrm{h}}, k_{\mathrm{v}})$ traces out a closed curve on the complex plane, and $v(k_{\mathrm{h}})$ counts the number of times it winds around the origin.

In addition, the chiral symmetry also ensures a quantized Zak phase [46] $\theta(k_{\mathrm{h}}) = \int_0^1 i \left\langle \psi(k_{\mathrm{v}}) | \nabla_{k_{\mathrm{v}}} \psi(k_{\mathrm{v}}) \right\rangle dk_{\mathrm{v}}$, which relates to the winding number through $\theta(k_{\mathrm{h}}) = |v(k_{\mathrm{h}})|\pi$. In Fig. 5(b), the blue line and red dots represent the Zak phase obtained from theoretical derivation and simulation calculation using the finite-element method (FEM),

respectively (see Appendix C for details), which indicate a nontrivial topological phase for the ZZ edge. In particular, $\theta(k_{\mathrm{h}}) = \pi$ accounts for a topologically nontrivial phase for $1/3 < k_{\mathrm{h}} < 2/3$. The degenerated bands cover one-third of the Brillouin zone. The borders correspond to the transition points when the 1D BZ passes through the reciprocal lattice sites K and K'. It is observed that the edge states between the unequal corners K and K' have topological protection properties.

The length of the finite ribbon does not affect the existence of edge states. Highly localized edge states exist even in the ribbon composed of two cells (see Appendix D for details). To demonstrate the propagation features of the edge states in a 2D ZZ ribbon, a simulation is conducted with the metamaterial plate described in Fig. 5(c), which consists of 12×10 cells in the ribbon. To make the manufacturing of this structure easier, the one-beam resonators on the left and right sides of the metamaterial boundaries are not considered in the calculations since their contribution is negligible. We use a point source located at the position defined by the green star to excite a harmonic flexural wave with frequency $f = 2060$ Hz. As shown in Fig. 5(c), the excited wave propagates along the boundary of the plate and decays almost exponentially into the interior. The color in the figure represents the distribution of out-of-plane displacement amplitude $|w|$. To verify the robust transmission of topological states along the free boundary of the elastic plate, we design two elastic plates with a size of 24×10 cells, as depicted in Figs. 5(e) and 5(f). In Fig. 5(f), a defect is introduced due to the absence of a single-beam oscillator on the upper boundary, which is indicated by the orange box. The localized vibration propagation can be observed on both free boundaries of the elastic plates. A cut line is drawn away from the point source, as shown by the green dashed line in Figs. 5(e) and 5(f). The total energy density W in the elastic plate decays rapidly as it moves away from the upper boundary, and the attenuation is the same in both elastic plates as shown in Fig. 5(d). The blue (ND) and orange (WD) dashed lines indicate the total energy density distribution along the cut line in the case of no defect and with defect, respectively. From Figs. 5(d)–5(f), it can be seen that after the introduction of the defect, the vibration distribution on the elastic plate has little impact, indicating that the transmission of edge states is robust to defects [27,55]. According to the previous discussion, edge states exist not only at the frequency defined by the Dirac point but also in a range of frequencies around the Dirac point.

F. Assessment of edge states by Shannon entropy

Entropy, which is the (log of the) number of microstates or microscopic configurations, has long been a concept in physics. In simple terms, if the particles inside a system have many possible positions to move around, the
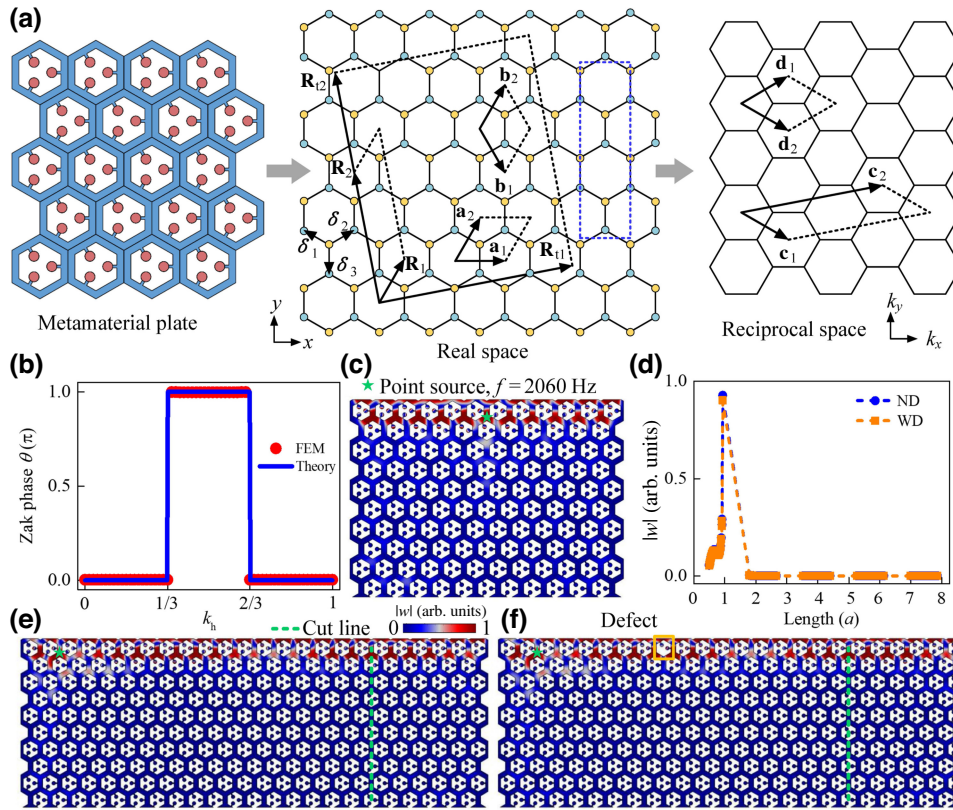
FIG. 5. (a) Two-dimensional elastic metamaterial plate with triangular lattice and graphenelike model. (b) Zak phase obtained from theoretical calculations (blue line, Theory) and simulation calculations [red dot, finite-element method (FEM)]. (c) The out-of-plane displacement field $|w|$ in the elastic plate. The color represents the distribution of normalized velocity amplitude, and the green star indicates the location of the point source. (d) The total energy density distribution along the cut line. The blue and orange dashed lines with symbols represent the variation of the total energy density on the cut lines without (ND) and with defects (WD), respectively. (e),(f) Distribution of displacement field $|w|$ in elastic plate without and with defects. The green pentagram represents the point source.

system has high entropy, and if they remain motionless, then the entropy of the system is low. Therefore, from the perspective of spatial distribution, the local and non-local characteristics of eigenmode distribution can also be characterized by entropy. Shannon proposed a computational method to quantify informational entropy, also known as Shannon entropy [56], which was first extended to atomic physics as [57] $S_u = -\int \rho_e(\mathbf{r}) \ln \rho_a(\mathbf{r}) d\mathbf{r}$, where $\rho_e(\mathbf{r}) = |\psi(\mathbf{r})|^2$ is the probability density distribution of a given electronic orbital, and more recently to acoustics [58]. Following the proposal in acoustics [58], we introduce here the "probability density function" for our metamaterial elastic plate: $P_s(\mathbf{r}) = V|u(\mathbf{r})|^2 / \int |u(\mathbf{r})|^2 d\mathbf{r}$, where $|u(\mathbf{r})|^2$ is the square norm of the total displacement field, which can be calculated as the dot product of the total displacement and its complex conjugate; V is the volume of the integration domain. The square norms of displacement are proportional to respective field intensities. Therefore, $P_s(\mathbf{r})$ plays the same role as $\rho_e(\mathbf{r})$ in electronic states. Following the definition of Shannon entropy in acoustics [58], to assess the spreading of localized elastic modes, we introduce the Shannon entropy as $S_u = -\int P_s(\mathbf{r}) \ln P_s(\mathbf{r}) d\mathbf{r}$.

This quantity provides a measure of the spatial delocalization of the modes in the system. The characteristic of Shannon entropy is that S_u increases with increasing uncertainty (i.e., increased spreading of the displacement field characterizing the eigenmode) [58].

Topological states have the characteristic of localization, and Shannon entropy can measure the degree of localization of the eigenmodes [58]. In graphenelike elastic plates, the topological states caused by the chiral symmetry of the Hamiltonian are related to the Dirac point [27,44], and there is a transition interval in the frequency of the edge states, so the frequency range of the edge states can be evaluated by Shannon entropy. Let us remark that in actual calculations, the volume in Shannon's entropy formula refers not to the total volume of the supercell, but to the volume of a single unit cell, which is proportional to the total volume. The two corners K and K' that support the Dirac point are located at the 1/3 and 2/3 segment points of the projected BZ, respectively. Therefore, to analyze the characteristics of the frequency band between the two corners K and K', without loss of generality, the larger wave vector interval selected here is from $k_x = 0.5$ to
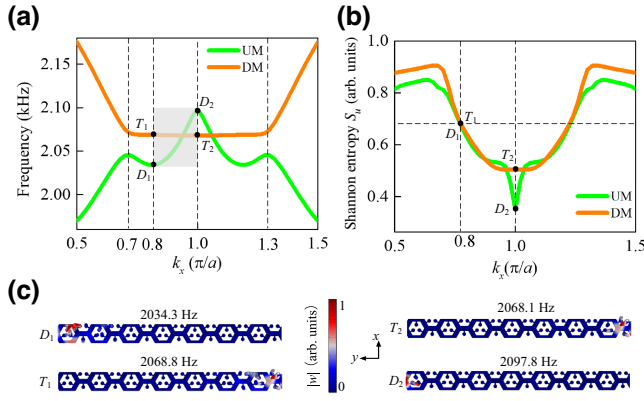
FIG. 6.   (a) Shannon entropy of edge modes belonging to the bands UM and DM. (b) Band structure for the bands UM and DM. (c) Displacement fields of eigenmodes D_1, T_1, D_2, and T_2 selected in (a).
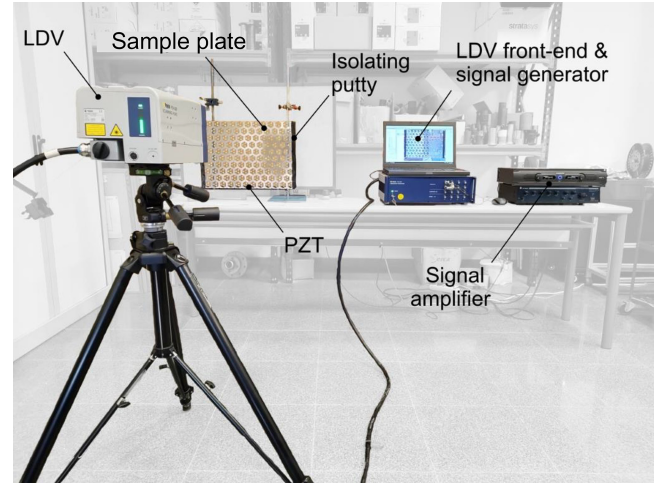

FIG. 7.   Experimental setup employed to characterize the flexural edge states propagating in the metamaterial plate under study, where LDV is a laser Doppler vibrometer and PZT is a piezoelectric transducer.

$k_x = 1.5$. For convenience, within the range of k_x from 0.5 to 1.5, the two segment bands are named UM in the band DB2 (with the edge states located at the top end of the ribbon), and DM in the band DB1 (with the edge states located at the bottom end of the ribbon), respectively, as shown in Fig. 6(a). It can be seen from the figure that for the DM segment, in the interval between $k_x = 0.7$ and 1.3, which are approximately the 1/3 and 2/3 dividing points of the 1D projection space, the frequency band is a flat band with a zero group velocity similar to that of graphite [38]. However, in the UM segment, the edge states localized at the top of the ribbon have a nonzero group velocity.

The Shannon entropy on the bands UM and DM is shown in Fig. 6(b). It is observed that Shannon entropy exhibits a symmetric distribution with respect to $k_x = 1$. As Shannon entropy increases, the vibrational modes extend into the supercell. Therefore, near $k_x = 1$, the eigenstates are highly localized. In order to determine the frequency range of the edge states, we assume that the displacement field of the edge states is localized within one cell near the end of the ribbon. In this case, when $|k_x - 1| \leq 0.2$, the eigenmode displacement field of the edge states satisfies this assumption; therefore, the range of wave vector k_x for the edge states is [0.8, 1.2]. Figure 6(c) shows the displacement fields of D_1 and T_1 at $k_x = 0.8$, and D_2 and T_2 at $k_x = 1$. From the distribution of the four modes, the vibrational energy is mainly localized in one cell at the upper or lower ends of the ribbon (the ribbon rotates counterclockwise by 90° in the figure). According to the Fig. 6(b), D_1 and D_2 are located in the band with nonzero group velocity, while the group velocity of T_1 or T_2 is close to zero, indicating that the frequencies of D_1 and D_2 can be used for signal propagation. Therefore, for the case of vibrational propagation, we consider these edge states with nonzero group velocity. It can be inferred that the frequency range of the edge states lies between D_1 and

D_2, [2034.3, 2097.8 Hz], as shown in the shaded area in Fig. 6(a). Interestingly, the frequency of the Dirac point is located near the center of the range. It is worth noting that, according to the assumption, the starting point of the edge state is D_1, and the Shannon entropy of the displacement field of mode D_1 is the same as that of T_1. Therefore, it can be concluded that the dashed line, as shown in Fig. 6(a), defines the wave vector range of the edge states. Under this criterion, the frequency range of the edge states for the gapless elastic plate can be determined. Additionally, the frequency of the edge states is influenced by the bulk state, so the actual frequency range of the propagating wave along the boundary may slightly differ from the predicted values.

III. EXPERIMENTAL OBSERVATION OF EDGE STATES

To verify the theoretical predictions regarding the propagation of flexural waves along the boundaries of the metamaterial plate under study, we use the experimental setup described in Fig. 7. In brief, we employ a Polytec PSV-500 scanning laser Doppler vibrometer (LDV) located 0.8 m away from the metamaterial sample. The sample plate shown in Fig. 7 had dimensions of about 480×350 mm^2 and was manufactured by laser-cutting using aluminum (Al-5745) with the same parameters (Young modulus and mass density) as those employed in the simulations. The accuracy of the laser-cutting technique used in manufacturing is about 0.1 mm [59]. The prototype was obtained from two aluminum sheets with a thickness of 1 and 4 mm, respectively; the designed metamaterial was cut from the former, and 4-mm-thick cylindrical pillars were obtained from the latter. Afterward, the pillars were attached with
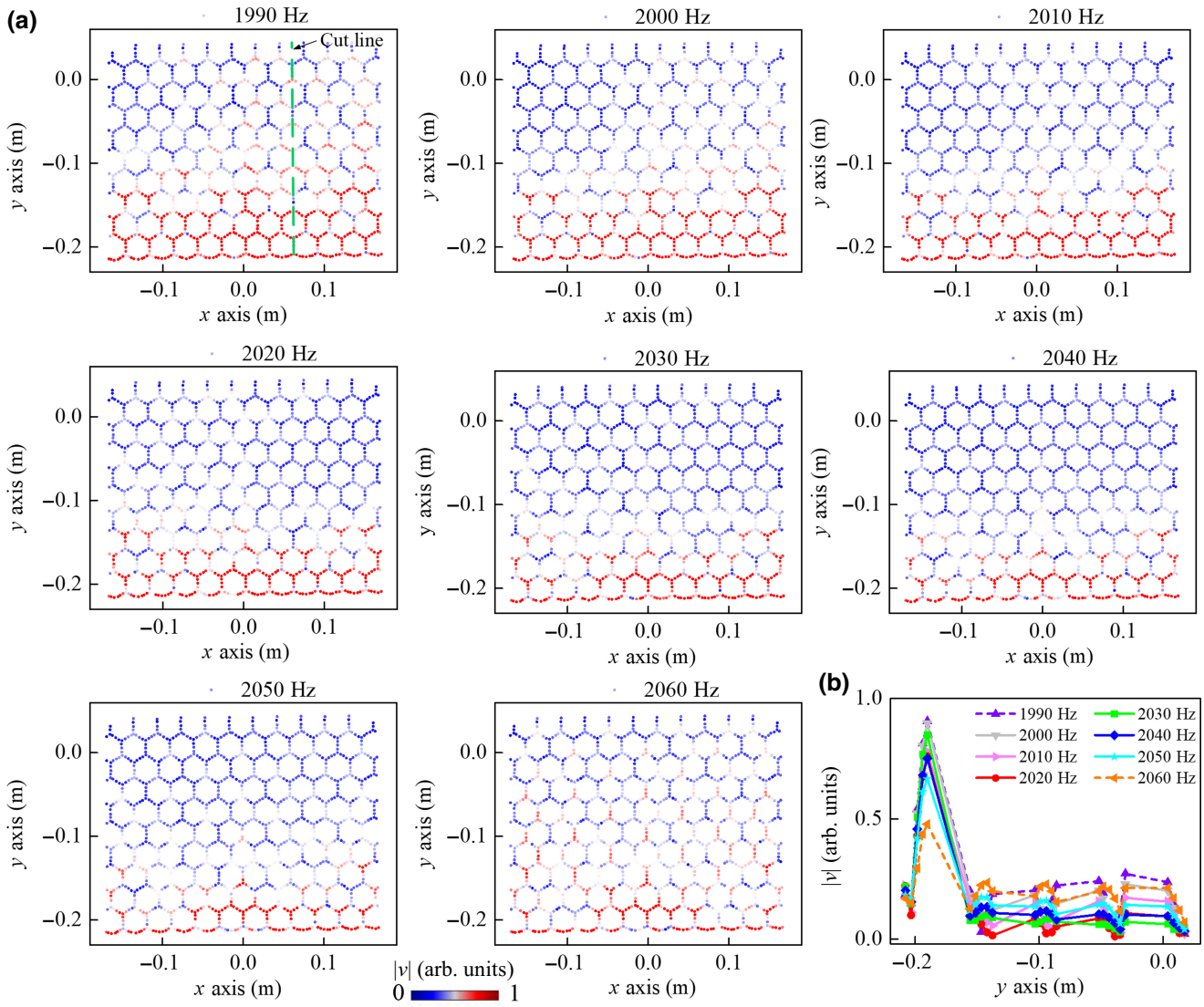
FIG. 8.   Distribution of velocity field. Color represents the distribution of velocity amplitude |v| in an elastic plate. (b) The velocity profile along the cut line. The lines with symbols represent the velocity amplitude along the cut line when the point source frequency is 1990, 2000, 2010, 2020, 2030, 2040, and 2050 Hz, respectively.

cyanoacrylate to their positions in the 1-mm-thick plate. The sample was installed vertically, hanging from two thin wires. In addition, mastic tape was added to the lateral boundaries to avoid possible wave reflections, thus mimicking the absorbing boundary condition employed in the numerical simulations.

Measurements are performed on the flat regions of the metamaterial sample plate (avoiding the cylindrical pillars), which have been discretized in roughly 1250 points. A computer audio card is employed to synthesize a sinusoidal signal, which is amplified with a 200-W Samson signal amplifier. The amplified electrical signal feeds a TDK PS1550L40N piezoelectric transducer with a diameter of 15 mm and a thickness of 1.6 mm, located as shown in

Fig. 7. The transducer excites flexural waves in the sample plate with the desired frequency. The measurements at each position of the grid are performed at a sampling rate of 16 kHz for 500 ms, repeated 3 times per sampling point in order to get an averaged result. The LDV system captures the propagation of excited flexural waves within the frequency range from 0 to 6.4 kHz, which, using 3200 fast Fourier transform lines, results in a frequency resolution of 2 Hz. Moreover, a passband filter is applied to the captured signal to filter out any unwanted interfering signal.

Figure 8 depicts the distribution of out-of-plane velocity fields when the excitation source frequency varies from 1990 to 2060 Hz in increments of 10 Hz. The figure illustrates that when the excitation frequency is

at 1990 and 2060 Hz, the flexural vibration can extend throughout the entire metamaterial plate. However, when the excitation source frequency is approximately in the range of 2010 to 2050 Hz (with a frequency interval of 40 Hz), the flexural waves primarily propagate locally at the free boundary. To distinguish the edge states from the bulk states in the experiment, we make a cut line on the elastic plate, which is represented by the green dashed line in Fig. 8(a). Figure 8(b) shows the variation curve of the velocity on the cut line, indicating that within the frequency range of 2010–2050 Hz, the vibration in the elastic plate is mainly localized near the boundary, and the vibration decays rapidly as it moves away from the boundary, showing the characteristics of the edge states. The experimental data demonstrate well that the topologically protected flexural edge states can propagate along the free boundaries of metamaterial plates [46].

The experimental test results in Fig. 8, when compared with the results obtained from finite-element calculations (see Appendix E for details), reveal that although the bandwidth of the topological edge states is roughly the same, the frequency of the edge states shifts down. There are three main reasons for this phenomenon. Firstly, the added glue increases the mass of the equivalent spring-mass model. Secondly, slight differences might exist between the parameters of the aluminum used in the simulations and the ones of actual aluminum employed in experiments. Finally, the number of finite elements used in the simulations just gives an approximation of the converged frequency. In addition, the simulations use the low-reflection condition (without mass) at the lateral sides of the plate. However, the experimental setup employs an absorbing material (with mass), which also produces a decrease of the measured frequencies.

IV. SUMMARY

We have demonstrated both theoretically and experimentally the existence of topologically protected edge states at the free borders of a graphenelike metamaterial plate, without breaking the time-reversal and inversion symmetry of the system. The topological edge states on the free boundary are not limited by the size of the finite structure, which can reduce the scale of the topological state system. In addition, the range of the topological edge states has been assessed using the elastic Shannon entropy. Our work can be extended to other elastic waves, such as shear waves, surface waves, etc. The results shown here foresee interesting engineering applications such as nondestructive testing and vibration isolation and open up alternative avenues for the study of topologically protected edge states in other classical waves such as electromagnetic waves.

V. METHODS

A. Numerical simulations and structure parameters

The numerical results presented in our work are performed in the framework of the fine-element method, using the commercial software, COMSOL Multiphysics. In addition, we employ the "Structural Mechanics module" to visualize the modal characteristics and propagating features of elastic waves. The material of the elastic plate is aluminum with the following physical parameters: Young's modulus $E = 70$ GPa, Poisson's ratio $\nu = 0.33$, and mass density $\rho = 2700$ kg/m^3. In the calculations of band structure, Floquet periodic boundary conditions are imposed on the periodic boundaries of the unit cell and the supercell. In the simulation of vibration propagation in the ribbon, low-reflection boundary conditions are imposed on the left and right boundaries of the ribbon, and the top and bottom boundaries are free. To calculate the Zak phase, the displacement field of the eigenstates at specific wave vectors is extracted from the numerical simulation of their eigenvalues. The parameters for Fig. 3(b) are $a = 40$ mm, $R = 0.35a$, and $h = 1$ mm. In Fig. 3(c), the parameters defining the resonator are $w_b = 2$ mm, $\ell = 10$ mm, $t = 1$ mm, and $d = 8$ mm. Figure 3(f) is calculated by the following structural parameters: $R = 0.75$, $r = 3.6$, and $L = 3.6$.

APPENDIX A: FLEXURAL WAVE VELOCITY AND FINITE-ELEMENT MESH

Considering only linearly elastic displacements, away from the source, the propagating waves in an elastic plate are governed by Lamb's homogeneous equation, whose solutions are called Lamb waves. When the wavelength is much larger than the plate thickness, a simpler set of governing equations derived from classical plate theory can be used to understand the motion. For thin plates, the waves have two modes of propagation. One is called the extensional and the other the flexural mode. Both have in-plane and out-of-plane components due to the Poisson effect. For the extensional mode, the larger component of its two displacement components is in the plane, while the larger component in the flexural mode is perpendicular to the plane of the plate [53].

For an isotropic plate, the extensional mode is analogous to the extensional wave in a rod, and just as in the case

of the rod, it is dispersionless. The (velocity) dispersion equation is

$$c_e = [E/(1 - \nu^2)\rho]^{1/2}, \qquad (A1)$$

where E is Young's modulus, ν is Poisson's ratio, and ρ is the density.

The flexural wave dispersion equation for the plate is analogous to flexural waves in an Euler beam and the velocity shows a similar dependence on the frequency. That is,

$$c_f = (D/\rho h)^{1/4} \omega^{1/2}, \qquad (A2)$$

where $D = Eh^3/12(1 - \nu^2)$, ω is the circular frequency, and h is the plate thickness. Note that the velocity c_f of flexural (bending) waves depends on frequency. In addition, since the theoretically obtained bending wave velocity does not consider the inertial effect and the shearing effect, there is a large deviation between the experimentally obtained bending wave velocity and the theoretical value [53].

For the flexural wave modes, the dispersion relation still varies as the square root of the frequency. Here, when referring to waves, the term flexural means displacement out of plane.

It is important to point out that the wave speeds are different for the types of modes propagating in the plate. For the in-plane modes, the wave speed in an aluminum plate is about twice as fast as the flexural mode at the highest flexural frequency measured, and, in the composite laminate, it is about 5 times as fast as the flexural mode. Combined with the nondispersive nature of the extensional mode, this enables the modes to be identified quite easily.

Considering the uncertainty of the vibration propagation speed in the plate, especially the bending wave speed, to obtain a converged solution, we select the ultrafine mesh (tetrahedral elements) to perform simulation calculations when using finite-element software to visualize the vibration situation in the periodic plate.

The convergence solution is obtained by reducing the maximum element size. The remaining grid size parameters include a minimum element size of 0.01 mm, maximum element growth rate of 1.3, curvature factor of 0.2, and narrow area resolution of 1. The convergence of the solution is introduced in Fig. 9. As the maximum unit size gradually decreases from 1.5 mm, in the triangular lattice unit cell, the slope of the relationship curve between Dirac point frequency and maximum unit size (blue line) gradually decreases, which means that the calculation results gradually converge, and the corresponding convergence frequency value is about 2.06 kHz. The green and orange lines respectively represent the degree of freedom of the solution and the time taken to solve a single frequency point. It is observed that when the maximum
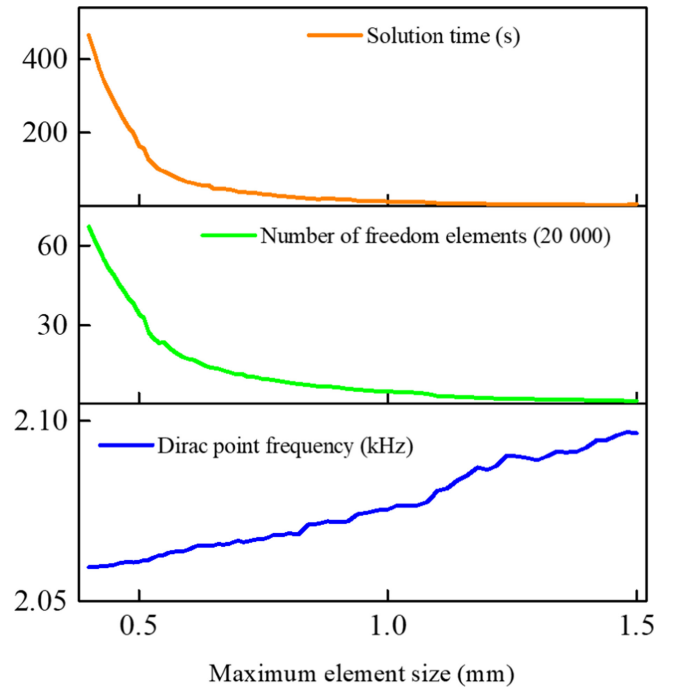

FIG. 9. The behavior of magnitudes of interest as a function of the maximum element size (in millimeters) employed in the finite-element calculations.

element size is less than 1 mm, the degree of freedom of the solution and the time for solving a single frequency point increase rapidly. Considering that when the maximum unit size is 0.8 mm, the Dirac point frequency is 2.066 kHz, which is very close to the convergence solution of 2.06 kHz, the maximum element size is 0.8 mm is used in the calculations described in the paper.

APPENDIX B: LOCAL RESONANT MODES INDUCED BY ONE-BEAM RESONATORS

It has been demonstrated that in resonant cavities containing one-beam resonators, the rectangular beam acts like a spring [50]. Therefore, the changes in the band structure introduced by the one-beam resonators can be easily explained by using a simple spring-mass model, where the beam attaching the disk to the plate plays the role of the spring, as shown in Fig. 10(a). The model developed here is similar to that applied by Goffaux and Sánchez-Dehesa [51] to explain the dispersion relation caused by a lattice of local resonators in 2D phononic materials. The model considers a lattice of masses connected by springs. Attached to each mass M, there exists a light pendulum (with mass m and length ℓ), which represents the localized mode associated with the one-beam resonator. This 1D mechanical system has an analytical solution and provides physical insight into the changes in the dispersion relations for both in-plane modes and out-of-plane modes produced by the hexagonal lattice of unit cells described in Fig. 10(a).
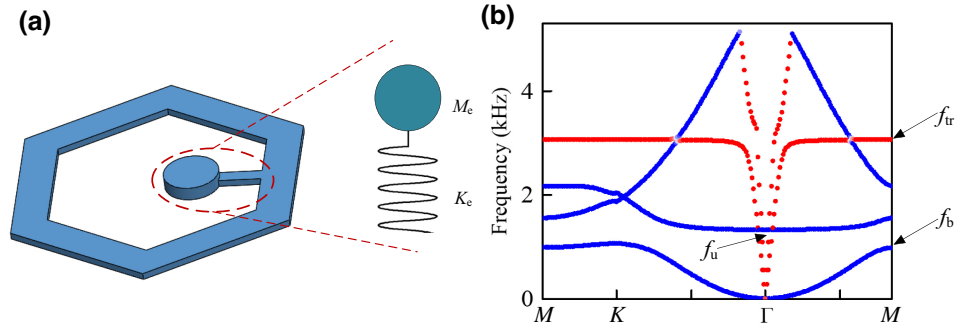
FIG. 10.   (a) Schematic diagram of the unit cell containing a single one-beam resonator, enclosed by the red dashed circle. The resonator can be modeled by a spring-mass system with effective mass M_e and effective spring stiffness K_e. (b) The corresponding dispersion relations for the in-plane (red dotted lines) and out-of-plane (blue lines) modes.

Figure 10(b) shows the dispersion relation of the out-of-plane modes (blue dotted lines) and the in-plane modes (red dotted lines) along the high-symmetry directions in the BZ of the hexagonal lattice. Let us first analyze the case of flexural (out-of-plane) modes. The band with an almost flat dispersion relation represents the band associated with the lattice of flexural local modes introduced by the one-beam resonator [see A in Fig. 3(d) in the main text]. Note that a band gap (gray region) occurs between the maximum frequency of the lower band f_b (located at the M point of the BZ), and the lowest frequency of the second band f_u (located at the Γ point of the BZ). The bandwidth $f_u - f_b$ gives an estimation of the interaction strength between the local resonant mode provided by the one-beam resonator and the continuum of flexural modes in the thin plate. Moreover, the interaction strength increases with the mass of the one-beam resonator [51], also producing a decrease in the mid-band-gap frequency [50].

The same analysis can be extended to understand the dispersion relations represented as red dotted lines, where the flat band is associated with the lattice of translational in-plane modes f_{tr} excited in the one-beam resonators [see Fig. 3(b) in the main text]. For these eigenmodes, the in-plane displacements of the one-beam resonators are much larger than that of the background plate. As for the case of flexural modes, a band gap (gray region) appears because of the interaction between the local resonance and the in-plane waves propagating in the plate.

Regarding the other types of local resonances produced by the one-beam resonator, like the torsional modes (f_{to}) and rotational modes (f_{ro}), their dispersion relations can be calculated, but they are located at much higher frequencies [50], and they are of no interest in this work.

APPENDIX C: EDGE STATES IN ZIGZAG RIBBONS

The intersection points between unit cells in the triangular lattice are abstracted as lattice points in a honeycomb lattice, as shown in Fig. 11(a), where $\mathbf{b}_1 = \left(1/2, \sqrt{3}/2\right) a$ and $\mathbf{b}_2 = \left(1/2, -\sqrt{3}/2\right) a$ represent the two basis vectors of the new honeycomb lattice. In addition, $\boldsymbol{\delta}_i$ ($i = 1$, 2, 3) denotes the vector between two inequivalent lattice points in the honeycomb lattice. The reciprocal lattice vectors of the honeycomb lattice are denoted as $\mathbf{d}_1 = 2\pi/a\left(1, 1/\sqrt{3}\right)$ and $\mathbf{d}_2 = 2\pi/a\left(1, -1/\sqrt{3}\right)$, as shown in Fig. 11(b). The Bloch wave vector $\mathbf{k}$ in the first Brillouin zone can be expressed as follows:

$$\mathbf{k} = k_h \mathbf{d}_1 + k_v \mathbf{d}_2, \quad k_h, k_v \in [0, 1). \quad \text{(C1)}$$

Next, we investigate the effective Hamiltonian of graphenelike elastic plates $H(\mathbf{k})$ [45],

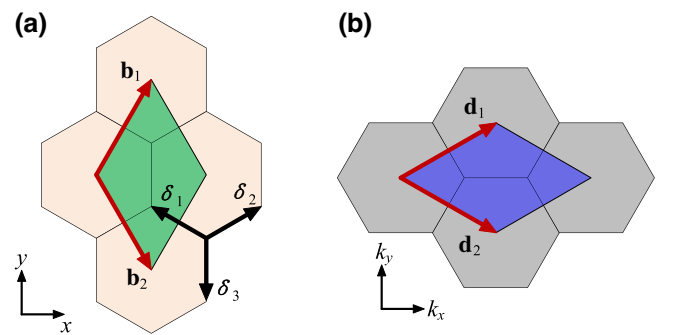$$H(\mathbf{k}) = [0, g(\mathbf{k}); g^*(\mathbf{k}), 0]. \quad \text{(C2)}$$

FIG. 11.   (a) The unit cell of the equivalent honeycomb lattice in the super unit cell of the triangular lattice. The orange color in the figure represents the triangular lattice, and the rhomboid green area represents the unit cell of the honeycomb lattice with $\mathbf{b}_1$ and $\mathbf{b}_2$ as basis vectors; the vectors connecting the adjacent nonequivalent lattice points in the honeycomb lattice are represented by $\boldsymbol{\delta}_i$ ($i = 1$, 2, 3). (b) The reciprocal lattice and the first Brillouin zone of the honeycomb lattice. The blue shading represents the first Brillouin zone with $\mathbf{d}_1$ and $\mathbf{d}_2$ as basis vectors.
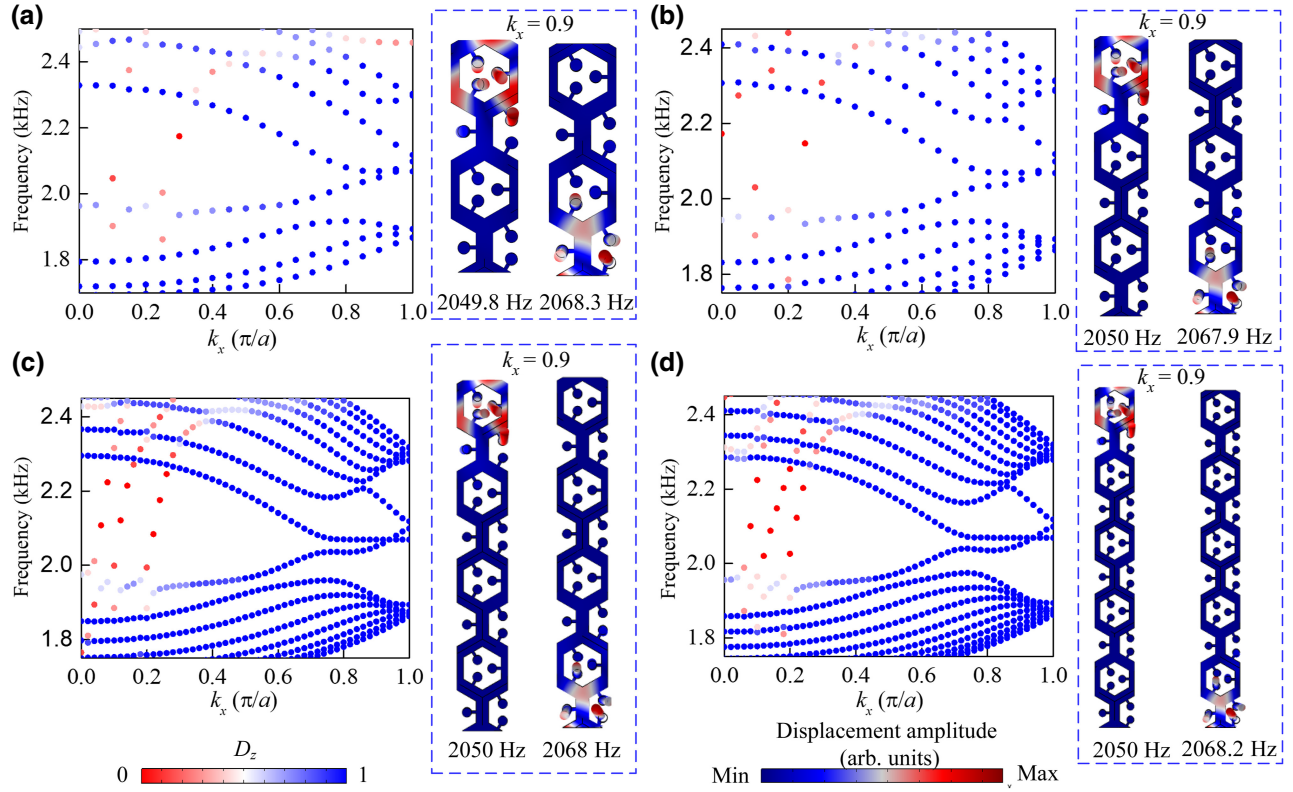
FIG. 12.   (a)–(d) Band structure and out-of-plane displacement fields of edge states at $k_x = 0.9$ calculated for ribbons composed of two, three, four, and five cells, respectively. The color in the band structure represents the out-of-plane mode polarizability, and the color in the modal distribution represents the displacement amplitude distribution.

Considering the relative phase of adjacent lattice points in a honeycomb lattice, the off-diagonal term $g(\mathbf{k})$ can be expressed as follows [45]:

$$g(\mathbf{k}) = 1 + e^{i\mathbf{k}\cdot(\boldsymbol{\delta}_3 - \boldsymbol{\delta}_2)} + e^{i\mathbf{k}\cdot(\boldsymbol{\delta}_3 - \boldsymbol{\delta}_1)}. \quad \text{(C3)}$$

Substituting Eq. (A1) into Eq. (C1),

$$g(k_{\mathrm{h}}, k_{\mathrm{v}}) = 1 + e^{-2\pi i k_{\mathrm{h}}} + e^{2\pi i k_{\mathrm{v}}}. \quad \text{(C4)}$$

For an elastic graphenelike plate, k_{h} can take arbitrary values ranging from 0 to 1, and the two-by-two effective Hamiltonian $H(\mathbf{k})$ can describe a 1D lattice model $H(k_{\mathrm{h}})$, when k_{v} runs through the 1D Brillouin zone for each k_{h}. Therefore, the winding number can be defined as follows [46]:

$$v(k_{\mathrm{h}}) = \frac{1}{2\pi i} \int_0^1 \frac{\partial \ln[g(k_{\mathrm{h}}, k_{\mathrm{v}})]}{\partial k_{\mathrm{v}}} dk_{\mathrm{v}}, \quad \text{(C5)}$$

where $g(k_{\mathrm{h}}, k_{\mathrm{v}})$ traces a closed curve in the complex plane and $v(k_{\mathrm{h}})$ represents the number of times it winds around the origin. Additionally, chiral symmetry also ensures the

quantized Zak phase [60],

$$\theta(k_{\mathrm{h}}) = \int_0^1 i \left\langle \psi(k_{\mathrm{v}}) | \nabla_{k_{\mathrm{v}}} \psi(k_{\mathrm{v}}) \right\rangle dk_{\mathrm{v}}, \quad \text{(C6)}$$

which relates to the winding number through the relation [5]

$$\theta(k_{\mathrm{h}}) = |v(k_{\mathrm{h}})|\pi. \quad \text{(C7)}$$

The theoretically calculated Zak phase, as shown by the blue line in Fig. 5(c), reveals that in the interval of $1/3 < k_{\mathrm{h}} < 2/3$, the Zak phase of the elastic plate with zigzag boundaries is π, which implies that the system is topologically nontrivial. In the simulation calculations, normalized displacements are used as eigenstates $\langle \psi(\mathbf{k})|$ and the Wilson-loop method is employed to compute the Zak phase of the system. Then $\mathbf{d}_1$ and $\mathbf{d}_2$ are discretized into N_1 and N_2 equal segments to satisfy the relations

$$\begin{aligned}
&k_{\mathrm{h},n} = \frac{n}{N_1} \\
&k_{\mathrm{v},m} = \frac{m}{N_2}
\end{aligned}, \quad n \in [0, 1, \quad N_1 - 1), m \in [0, 1, \quad N_2 - 1). \quad \text{(C8)}$$

For each $k_{\mathrm{h},n}$, the Zak phase is the sum of the Berry phases in all small segments (from $k_{\mathrm{v},m}$ to $k_{\mathrm{v},m+1}$) in the
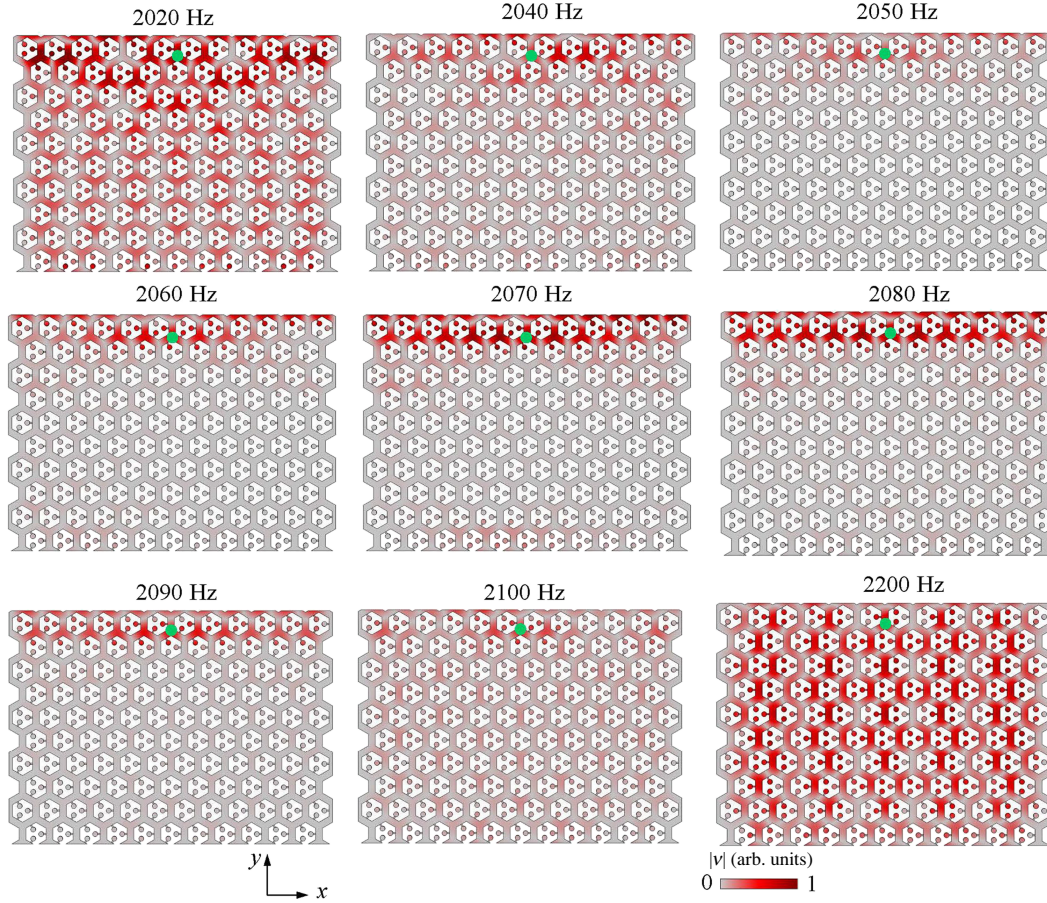
FIG. 13. The distribution of velocity fields for different excitation frequencies of the point source. The green dot indicates the position of the point source.

$\mathbf{d}_2$ direction, which can be expressed as follows:

$$e^{-i\theta_{k_h}} = \prod_{m=0}^{N_2-1} e^{-i\theta_{k_{v,m}}} = \prod_{m=0}^{N_2-1} \langle \psi(k_{v,m})|\psi(k_{v,m+1})\rangle. \quad (C9)$$

By calculating the Zak phase of the Bloch wave function represented by displacement on the compressed 1D space, as shown by the red dots in Fig. 5(c), we can see the distribution of the Zak phase on the fourth band (located near the Dirac point) is the same as the theoretically calculated value; i.e., in the interval of $1/3 < k_h < 2/3$, the system has a nontrivial phase and supports topological edge states. In fact, within the interval of k_h, the transition point between the topological trivial phase and topological nontrivial phase corresponds to the corner points K and K' in the first Brillouin zone. Therefore, in the projected band structure, the edge states located between K and K' are topologically protected.

To avoid the existence of a single-beam oscillator at the boundary and affecting the processing accuracy of the sample, in the finite structure we move the rectangular area in the model a certain distance along the y

axis. This movement will affect the chiral symmetry of the Hamiltonian; however, the edge states still exist under the protection of the approximate chiral symmetry [46].

APPENDIX D: EDGE STATES IN ZIGZAG RIBBONS MADE OF N CELLS

A double degenerate band occurs at the frequency of the Dirac point, and the edge states on this band are topologically protected. Figure 12 shows numerical simulations demonstrating that the edge states contained in the band structure of ribbons are independent of the number N of cells contained in the 1D ribbon.

The left panels in Figs. 12(a)–(d) show the band structure obtained with a supercell composed of two, three, four, and five cells, respectively. The right panels represent the corresponding out-of-plane displacement fields of the eigenmodes with frequencies belonging to the up and down bands containing edge states at $k_x = 0.9$. The displacement in Fig. 12 shows that the out-of-plane displacements are always localized at the top or bottom boundaries of the ribbon, although this ribbon is composed of just two cells. The fact that ribbons with smaller dimensions

can generate edge states provides a feasible solution for greatly reducing the sample size and realizing functional integration design and other engineering applications.

APPENDIX E: PROPAGATION IN A METAMATERIAL PLATE

To analyze the propagation of flexural waves in a metamaterial plate, a thin plate consisting of 12 supercells containing five cells is selected as shown in Fig. 13. A low reflection boundary condition is applied to the left and right boundary of the metamaterial plate, and the upper and lower boundary remain free.

We apply harmonic vibration excitation at the upper part of the plate, represented by the green circles in the illustration. Figure 13 displays the distribution of out-of-plane velocity fields for excitation source frequencies of 2020, 2040, 2050, 2060, 2070, 2080, 2090, 2100, and 2200 Hz. This figure shows that when the excitation source frequency is below 2050 Hz or above 2090 Hz, the vibration can extend throughout the entire metamaterial plate. When the frequency is between 2050 and 2090 Hz (with a bandwidth of approximately 40 Hz), flexural wave vibrations propagate along the free boundary of the metamaterial plate, demonstrating robustness in transmission. In addition, the vibration excited by the point source with a frequency of 2070 Hz can propagate along the top boundary of the plate, and at the bottom boundary of the plate, there is a local mode vibration. This is because the eigenmodes (near the Dirac point) at the frequency of 2070 Hz exhibit a strong local resonance pattern at the bottom end of the ribbon, as shown in Fig. 4(e). Therefore, the weak vibration propagating to the bottom boundary is strengthened. When the frequency is near the Dirac point, such as at 2070 Hz, once the excitation is applied to the top end of the metamaterial plate, there will also be weak local vibration at the bottom end of the metamaterial plate. This phenomenon can be used to judge the Dirac point frequency of the system in practical applications and is useful to estimate the range of edge states.

---

[1] J. Hu, Z. Chang, and G. Hu, Approximate method for controlling solid elastic waves by transformation media, Phys. Rev. B **84**, 201101 (2011).

[2] J. Zhang, W. Rui, C. Ma, Y. Cheng, X. Liu, and J. Christensen, Remote whispering metamaterial for non-radiative transceiving of ultra-weak sound, Nat. Commun. **12**, 3670 (2021).

[3] F. Ma, H. Zhang, X. Wang, C. Liu, and J. H. Wu, Ultrathin space-shift phase-coherent cancellation metasurface for broadband sound absorption, Small Methods **7**, 2300569 (2023).

[4] R. Zhu, X. N. Liu, G. K. Hu, C. T. Sun, and G. L. Huang, Negative refraction of elastic waves at the deep-subwavelength scale in a single-phase metamaterial, Nat. Commun. **5**, 5510 (2014).

[5] Y. Wu, Y. Lai, and Z.-Q. Zhang, Elastic metamaterials with simultaneously negative effective shear modulus and mass density, Phys. Rev. Lett. **107**, 105506 (2011).

[6] D. Bigoni, S. Guenneau, A. B. Movchan, and M. Brun, Elastic metamaterials with inertial locally resonant structures: Application to lensing and localization, Phys. Rev. B **87**, 174303 (2013).

[7] M. Farhat, S. Guenneau, and S. Enoch, Ultrabroadband elastic cloaking in thin plates, Phys. Rev. Lett. **103**, 024301 (2009).

[8] D. J. Thouless, M. Kohmoto, M. P. Nightingale, and M. Den Nijs, Quantized Hall conductance in a two-dimensional periodic potential, Phys. Rev. Lett. **49**, 405 (1982).

[9] X. L. Qi and S. C. Zhang, Topological insulators and superconductors, Rev. Mod. Phys. **83**, 1057 (2011).

[10] C. L. Kane and E. J. Mele, Quantum spin Hall effect in graphene, Phys. Rev. Lett. **95**, 226801 (2005).

[11] D. Xiao, W. Yao, and Q. Niu, Valley-contrasting physics in graphene: Magnetic moment and topological transport, Phys. Rev. Lett. **99**, 236809 (2007).

[12] D. Hsieh, D. Qian, L. Wray, Y. Xia, Y. S. Hor, R. J. Cava, and M. Z. Hasan, A topological Dirac insulator in a quantum spin Hall phase, Nature **452**, 970 (2008).

[13] Y. L. Chen, J. G. Analytis, J.-H. Chu, Z. K. Liu, S.-K. Mo, X. L. Qi, H. J. Zhang, D. H. Lu, X. Dai, Z. Fang, *et al.*, Experimental realization of a three-dimensional topological insulator, Bi_2Te_3, Science **325**, 178 (2009).

[14] J. E. Moore, The birth of topological insulators, Nature **464**, 194 (2010).

[15] M. Kim, Z. Wang, Y. Yang, H. T. Teo, J. Rho, and B. Zhang, Three-dimensional photonic topological insulator without spin-orbit coupling, Nat. Commun. **13**, 3499 (2022).

[16] Su-Yang Xu, Y. Xia, L. A. Wray, D. Qian, Shuang Jia, J. H. Dil, F. Meier, J. Osterwalder, B. Slomski, H. Lin, R. J. Cava, and M. Z. Hasan, Topological phase transition and texture inversion in a tunable topological insulator, Science **332**, 560 (2011).

[17] L. Fu, Topological crystalline insulators, Phys. Rev. Lett. **106**, 106802 (2011).

[18] P. S. Mandal, G. Springholz, V. V. Volobuev, O. Caha, A. Varykhalov, E. Golias, G. Bauer, O. Rader, and J. Sanchez-Barriga, Topological quantum phase transition from mirror to time reversal symmetry protected topological insulator, Nat. Commun. **8**, 968 (2017).

[19] P. Wang, L. Lu, and K. Bertoldi, Topological phononic crystals with one-way elastic edge waves, Phys. Rev. Lett. **115**, 104302 (2015).

[20] L. M. Nash, D. Kleckner, A. Read, V. Vitelli, A. M. Turner, and W. T. Irvine, Topological mechanics of gyroscopic metamaterials, Proc. Natl. Acad. Sci. **112**, 14495 (2015).

[21] X. Zhang, F. Zangeneh-Nejad, Z. G. Chen, M. H. Lu, and J. Christensen, A second wave of topological phenomena in photonics and acoustics, Nature **618**, 687 (2023).

[22] Z. Huang, J. H. Wu, Y. Z. Lei, C. R. Liu, and F. Y. Ma, Multi-band acoustic topological insulator, Mater. Today Phys. **27**, 100793 (2022).

[23] R. Süsstrunk and S. D. Huber, Observation of phononic helical edge states in a mechanical topological insulator, Science **349**, 47 (2015).

[24] L. Y. Zheng, G. Theocharis, V. Tournat, and V. Gusev, Quasitopological rotational waves in mechanical granular graphene, Phys. Rev. B **97**, 060101 (2018).

[25] S. H. Mousavi, A. B. Khanikaev, and Z. Wang, Topologically protected elastic waves in phononic metamaterials, Nat. Commun. **6**, 8682 (2015).

[26] Si-Yuan Yu, Cheng He, Zhen Wang, Fu-Kang Liu, Xiao-Chen Sun, Zheng Li, Hai-Zhou Lu, Ming-Hui Lu, Xiao-Ping Liu, and Yan-Feng Chen, Elastic pseudospin transport for integratable topological phononic circuits, Nat. Commun. **9**, 3072 (2018).

[27] Y. Wu, J. Y. Lu, X. Q. Huang, and Y. Y. Ting, Topological materials for full-vector elastic waves, Natl. Sci. Rev. **10**, nwac203 (2022).

[28] S. Y. Huo, J. J. Chen, and H. B. Huang, Topologically protected edge states for out-of-plane and in-plane bulk elastic waves, J. Phys.: Condens. Matter **30**, 145403 (2018).

[29] J. Cha, K. W. Kim, and C. Daraio, Experimental realization of on-chip topological nanoelectromechanical metamaterials, Nature **564**, 229 (2018).

[30] J. Vila, R. K. Pal, and M. Ruzzene, Observation of topological valley modes in an elastic hexagonal lattice, Phys. Rev. B **96**, 134307 (2017).

[31] M. Yan, J. Lu, F. Li, W. Deng, X. Huang, J. Ma, and Z. Liu, On-chip valley topological materials for elastic wave manipulation, Nat. Mater. **17**, 993 (2018).

[32] S. F. Li and J. Yang, Topological transition in spiral elastic valley metamaterials, Phys. Rev. Appl. **15**, 014058 (2021).

[33] S. F. Li, I. Kim, S. Iwamoto, J. F. Zang, and J. Yang, Valley anisotropy in elastic metamaterials, Phys. Rev. B **100**, 195102 (2019).

[34] Y. F. Chen, Z. G. Chen, H. Ge, C. He, X. Li, M. H. Lu, X. C. Sun, S. Y. Yu, and X. Zhang, Various topological phases and their abnormal effects of topological acoustic metamaterials, Interdiscip. Mater. **2**, 179 (2023).

[35] X. Shi, R. Chaunsali, F. Li, and J. Yang, Elastic Weyl points and surface arc states in three-dimensional structures, Phys. Rev. Appl. **12**, 024058 (2019).

[36] K. Wakabayashi, M. Fujita, H. Ajiki, and M. Sigrist, Electronic and magnetic properties of nanographite ribbons, Phys. Rev. B **59**, 8271 (1999).

[37] D. Torrent, D. Mayou, and J. Sánchez-Dehesa, Elastic analog of graphene: Dirac cones and edge states for flexural waves in thin plates, Phys. Rev. B **87**, 115143 (2013).

[38] M. Fujita, K. Wakabayashi, K. Nakada, and K. Kusakabe, Peculiar localized state at zigzag graphite edge, J. Phys. Soc. Jpn. **65**, 1920 (1996).

[39] J. Y. Lu, C. Y. Qiu, L. P. Ye, X. Y. Fan, M. Z. Ke, F. Zhang, and Z. Y. Liu, Observation of topological valley transport of sound in sonic crystals, Nat. Phys. **13**, 369 (2016).

[40] C. He, X. Ni, H. Ge, X. C. Sun, Y.-B. Chen, M.-H. Lu, X.-P. Liu, and Y.-F. Chen, Acoustic topological insulator and robust one-way sound transport, Nat. Phys. **12**, 1124 (2016).

[41] K. Sasaki, M. Suzuki, and R. Saito, Aharanov-Bohm effect for the edge states of zigzag carbon nanotubes, Phys. Rev. B **77**, 045138 (2008).

[42] K. Wakabayashi, M. Sigrist, and M. Fujita, Spin wave mode of edge-localized magnetic states in nanographite zigzag ribbons, J. Phys. Soc. Jpn. **67**, 2089 (1998).

[43] S. Lin, G. Zhang, C. Li, and Z. Song, Magnetic-flux-driven topological quantum phase transition and manipulation of perfect edge states in graphene tube, Sci. Rep. **6**, 31953 (2016).

[44] W. Izumida, L. Milz, M. Marganska, and M. Grifoni, Topology and zero energy edge states in carbon nanotubes with superconducting pairing, Phys. Rev. B **96**, 125414 (2017).

[45] R. Okuyama, W. Izumida, and M. Eto, Topological classification of the single-wall carbon nanotube, Phys. Rev. B **99**, 115409 (2019).

[46] Z. Zhang, P. Gao, W. Liu, Z. Yue, Y. Cheng, X. Liu, and J. Christensen, Structured sonic tube with carbon nanotube-like topological edge states, Nat. Commun. **13**, 5096 (2022).

[47] J. Y. Lu, C. Y. Qiu, S. J. Xu, Y. T. Ye, M. Z. Ke, and Z. Y. Liu, Dirac cones in two-dimensional artificial crystals for classical waves, Phys. Rev. B **89**, 134302 (2014).

[48] Z. Huang, J. Wu, C. Wang, S. Yang, and F. Ma, Resonant-scattering hybrid device for multiband acoustic topology valley transmission, Phys. Rev. B **104**, 094110 (2021).

[49] A. Ni and Z. Shi, Topological metamaterial plates: Numerical investigation, experimental validation and applications, Eng. Struct. **275**, 115288 (2023).

[50] P. Gao, A. Climente, J. Sanchez-Dehesa, and L. Wu, Theoretical study of platonic crystals with periodically structured N-beam resonators, J. Appl. Phys. **123**, 091707 (2018).

[51] C. Goffaux and J. Sánchez-Dehesa, Two-dimensional phononic crystals studied using a variational method: Application to lattices of locally resonant materials, Phys. Rev. B **67**, 144301 (2003).

[52] A. H. Castro Neto, F. Guinea, N. M. R. Peres, K. S. Novoselov, and A. K. Geim, The electronic properties of graphene, Rev. Mod. Phys. **81**, 109 (2009).

[53] M. R. Gorman, Plate wave acoustic emission, J. Acoust. Soc. Am. **90**, 358 (1991).

[54] L. Y. Zheng, F. Allein, V. Tournat, Vitalyi Gusev, and G. Theocharis, Granular graphene: Direct observation of edge states on zigzag and armchair boundaries, Phys. Rev. B **99**, 184113 (2019).

[55] Z. Wen, S. Zeng, D. Wang, Y. Jin, and B. Djafari-Rouhani, Robust edge states of subwavelength chiral phononic plates, Extreme Mech. Lett. **44**, 101209 (2021).

[56] C. E. Shannon, A mathematical theory of communication, Bell Syst. Tech. J. **27**, 379 (1948).

[57] R. Gonzalez-Ferez and J. S. Dehesa, Shannon entropy as an indicator of atomic avoided crossings in strong parallel magnetic and electric fields, Phys. Rev. Lett. **91**, 113001 (2003).

[58] J. Sánchez-Dehesa and J. R. Arias-Gonzalez, Characterization of avoided crossings in acoustic superlattices: The Shannon entropy in acoustics, Front. Phys. **10**, 971171 (2022).

[59] J. Sánchez-Dehesa, P. Gao, F. Cervera, A. Broatch, J. García-Tíscar, and A. Felgueroso, Experimental evidence of the Poisson-like effect for flexural waves in thin metallic plates, Appl. Phys. Lett. **120**, 094102 (2022).

[60] H. X. Wang, G. Y. Guo, and J. H. Jiang, Band topology in classical waves: Wilson-loop approach to topological numbers and fragile topology, New J. Phys. **21**, 093029 (2019).